nature astronomy

Article

https://doi.org/10.1038/s41550-026-02815-8

Volatile-rich evolution of molten super-Earth L 98-59 d

Received: 29 May 2025

Accepted: 18 February 2026

Published online: 16 March 2026

Check for updates

Harrison Nicholls[1,2] ✉, Tim Lichtenberg[3], Richard D. Chatterjee[1,4], Claire Marie Guimond[1,5], Emma Postolec[3] & Raymond T. Pierrehumbert[1]

Small, low-density exoplanets are sculpted by strong stellar irradiation, but their primordial compositions and subsequent evolution are still unknown. Two often-considered scenarios hold that they formed with rocky interiors and H_2–He atmospheres ('gas dwarfs') or alternatively with bulk compositions dominated by H_2O phases ('water worlds'). Here we constrain the possible range of evolutionary histories linking the birth conditions of low-density super-Earth L 98-59 d to recent observations using a coupled atmosphere–interior evolutionary model. We find that the observations can be explained by in situ photochemical production of SO_2 in an H_2 background, indicative of a chemically reducing mantle and substantial (>1.8 mass%) early sulfur and hydrogen content, inconsistent with both the gas-dwarf and water-world scenarios. L 98-59 d's interior comprises a permanent magma ocean, allowing long-term retention of volatiles within its mantle over billions of years, consistent with California-Kepler Survey trends. Our analysis reveals an evolutionary pathway in which planets host volatile-rich atmospheres sustained by long-term magma-ocean degassing, shaped by secular cooling, atmospheric erosion and photochemistry. Internal and environmental processes contribute to the observed diversity of super-Earth and sub-Neptune exoplanets.

Exoplanets with radii between ~1.5 $R_\oplus$ and ~4.0 $R_\oplus$ are abundant and amenable to characterization using current instruments, yet they have no Solar System analogues[1]. This small-planet regime includes the super-Earth and sub-Neptune populations, between which there exists an apparent paucity in the surveyed population known as the 'radius valley', although it remains unclear how these exoplanet populations originate[2,3]. Two separate scenarios are often considered to explain the properties of these planets[4,5]: (1) gas dwarfs, where both populations jointly form with large H_2-dominated envelopes and then diverge into two distinct populations due to long-term atmospheric escape processes[6,7]; and (2) water worlds, where super-Earths and sub-Neptunes differ in H_2O content obtained from formation relative to the ice line[8–11]. Combinations of both scenarios may explain the emergence of sub-Neptunes and super-Earths on a population level, but not on an individual-planet basis[12,13]. An apparent over-abundance of young sub-Neptune planets may represent a reservoir of future super-Earths, which, if true, intimately links these two proposed populations across the radius valley[3,14].

L 98-59 hosts three transiting exoplanets[15,16]. Hubble Space Telescope observations of the innermost sub-Venus planet rule out a low-mean-molecular-weight (MMW) primary atmosphere[17], but recent James Webb Space Telescope (JWST) transit spectroscopy has indicated an SO_2-rich atmosphere[18], raising the possibility of an S-rich planetary system. Hubble Space Telescope observations of the outermost transiting planet (L 98-59 d) have also ruled out a pure H_2 atmosphere[19]. Yet L 98-59 d's exceptionally low bulk density, recently estimated as 2.2 g cm^{-3} (with mass 1.64 $M_\oplus$ and radius 1.627 $R_\oplus$), is inconsistent with a pure rock-and-iron composition and is instead consistent with it

[1]Department of Physics, University of Oxford, Oxford, UK. [2]Institute of Astronomy, University of Cambridge, Cambridge, UK. [3]Kapteyn Astronomical Institute, University of Groningen, Groningen, the Netherlands. [4]School of Physics and Astronomy, University of Leeds, Leeds, UK. [5]Department of Earth and Planetary Sciences, ETH Zürich, Zürich, Switzerland. ✉e-mail: harrison.nicholls@ast.cam.ac.uk

https://doi.org/10.1038/s41550-026-02815-8

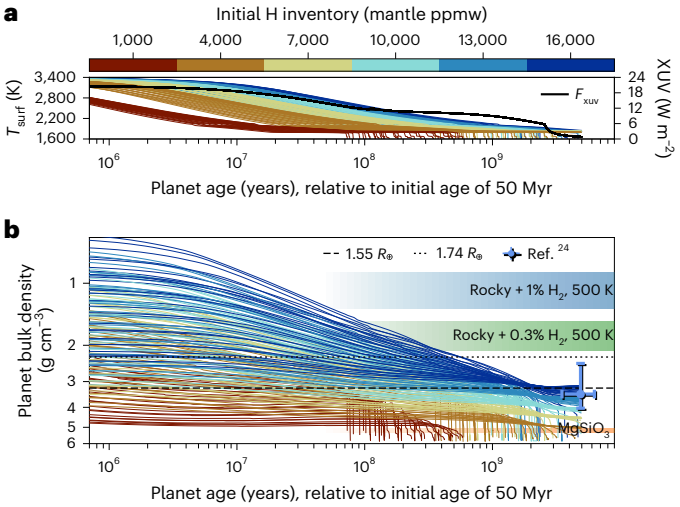

Fig. 1 | Temporal evolution of L 98-59 d's bulk density simulated over its lifetime. a, Initial hydrogen inventory (mantle ppmw) of each bulk-density evolution track is shown by the line colour. Blue/green shaded regions are reference densities for a planet of this mass[5]. Black dashed/dotted lines demarcate edges of the radius valley (at this planet mass) for low-mass stars. The region $\pm1\sigma$ compatible with the estimated bulk density of this planet is indicated by the blue error bar[15,24]. **b**, Evolution of surface temperature (coloured) and stellar XUV energy flux (black). For visual clarity, this figure only shows cases with S/H = 8.

hosting substantial atmosphere-forming volatiles[15,20]. Retrievals on its transit spectrum point to an atmosphere of sulfur-bearing volatiles (H_2S, SO_2) within a background of H_2. Free-chemistry models fit at 5.6σ with a MMW of $9.18^{+2.51}_{-2.41}$ g mol^{-1} and an H_2S volume mixing ratio of $10^{-0.74^{+0.14}_{-0.49}}$ (ref. 21). However, thermochemical equilibrium models fit with a MMW of $32.13^{+1.50}_{-8.31}$ g mol^{-1} at a lower significance of only 2.7σ. Retrievals also place weak constraints on H_2O, CO_2 and CH_4 (ref. 22). Sitting proximate to the radius valley, L 98-59 d stands out among the low-mass exoplanets as prime for tracing the physics of rocky planet formation and evolution[23].

Here, we constrain the plausible set of evolutionary pathways for L 98-59 d by numerically linking its birth conditions to recent estimates of its bulk density ρ_p and atmospheric composition. For this comparison, we primarily adopt $\rho_p = 3.45$ g cm^{-3} previously estimated by Rajpaul et al.[24] and the corresponding upper-atmospheric composition constraints from JWST[21,22]. An alternative recent estimate of a smaller $\rho_p = 2.2$ g cm^{-3} is simultaneously explored[20] (Supplementary Table 1). We use the PROTEUS modelling framework to create a large grid of self-consistent coupled atmosphere–interior evolutionary simulations to compare with observational constraints[25–28]. PROTEUS calculates the evolving thermochemical state of the planet's interior and atmosphere over time. From a molten start, we simultaneously model bottom-up mantle crystallization, tidal dissipation, outgassing and escape of CHNOS volatiles, atmospheric blanketing and energy transport and stellar evolution. Our radiative–convective atmosphere implements a real-gas equation of state (EOS) and correlated-k radiative transfer and allows the formation of deep radiative layers[27,29]. Stellar X-rays and extreme ultraviolet (XUV) fluxes are used to calculate the rate of volatile loss (Methods) using an energy-limited hydrodynamic escape parametrization[30]. Our main grid of 900 models has four axes: initial volatile endowment (proxied as hydrogen relative to the total mantle mass, $1{,}000 \leq H_{ppmw} \leq 16{,}000$), bulk S/H mass ratio, magma-ocean oxygen fugacity and total planet mass. The grid domain spans a range of post-accretion scenarios as planets are thought to vary substantially in their initial amount of volatiles[5,31] in addition to variations their mantle redox state[1,32], which controls the solubility of volatiles in silicate melt and chemical speciation throughout the planet[33,34]. Models terminate at the planet's estimated age of (4.94 ± 1.44) Gyr or at mantle solidification; we do not model secondary volcanic outgassing from magmatism during solid-state mantle convection. PROTEUS simulation end points are compared with observational constraints on the planet's density[24] and atmospheric MMW[21] to infer L 98-59 d's thermal and compositional history.

A volatile-rich birth

Modelled evolutionary tracks (Fig. 1b) show that the bulk density ρ_p of L 98-59 d has changed substantially over its lifetime. For larger initial volatile inventories (blue lines), ρ_p is typically less than 2 g cm^{-3} during the first several Myr of evolution. The planet's observable effective radius (R_p; Methods) initially exceeds the 1.7 $R_\oplus$ value often taken as the transition between the super-Earth and sub-Neptune regimes. Some models remain deep within the sub-Neptune regime ($R_p \geq 1.7\ R_\oplus$) for 950 Myr. Radiative energy losses drive initial cooling and atmospheric contraction, causing the planet's radius to shrink below the upper edge of the radius valley (dotted line, Fig. 1b). Irreversible loss of CNHOS volatiles through XUV-driven photoevaporation dominates the planet's bulk-density evolution at later times up to the present. Scenarios that fall within estimates of the present-day ρ_p (ref. 24) are all initially volatile rich: $H_{ppmw} \gtrsim 13{,}000$ with CHNOS volatiles making up $\gtrsim$1.8% of the planet's mass.

The mantle solidifies under volatile-poorer formation scenarios (Fig. 1b, maroon lines) from 70 Myr onwards. Surface cooling and near-complete escape of degassed volatiles lead to an increase in ρ_p towards that of a rocky composition within 650 Myr. These volatile-stripped scenarios are not compatible with the observed ρ_p despite initial H contents likely larger than those of the inner Solar System planets[35]. These cases, applicable to high-density exoplanets not modelled here, reflect suggestions that airless exoplanets may be the stripped interiors of evolved sub-Neptunes[7,36].

Which scenarios are compatible with the observations? Figure 2 plots modelled ρ_p at ages corresponding to the present day. Values of ρ_p are projected over the grid axes (Fig. 2a–d) and other variables. All cases compatible with the ρ_p estimated by Rajpaul et al.[24] (orange points) exhibit MMWs from 7 to 24 g mol^{-1} (Fig. 2e), a spread wider than the $\pm1\sigma$ range of $9.18^{+2.51}_{-2.41}$ g mol^{-1} (purple line) derived with JWST[21]. Simultaneously applying the density and MMW constraints yields the smaller set of blue points.

Formation with $H_{ppmw} < 10{,}000$ can be readily ruled out on the basis of ρ_p alone (grey points in Fig. 2). Here, we compare our model against the maximum estimate of ρ_p in the literature, so this conclusion is insensitive to the quoted uncertainty in ρ_p. Larger escape efficiencies, or lower bulk densities, such as recently estimated by Cadieux et al.[20], necessitate birth scenarios that are even more volatile-rich to satisfy the present-day ρ_p (Supplementary Fig. 1).

Figure 2b shows that magma-ocean oxygen fugacity fO_2 (expressed in log-units relative to the iron-wüstite (IW) buffer) must be between IW − 4 and IW − 1 to reproduce the estimated ρ_p and MMW. More oxidizing conditions favour gas speciation towards O-bearing species, increasing the atmospheric MMW. A modest MMW (~9 g mol^{-1}) lowers the atmosphere's propensity for escape through a decreased radius. Larger MMW atmospheres are either over-dense or inconsistent with the JWST transit depths (or both). The full range of initial S/H mass ratio modelled is compatible with the observed ρ_p. Variations in the planet's dry mass itself have only minor impact on the modelled ρ_p compared to the other variables, which drive changes in its radius R_p (Supplementary Fig. 2).

All outcomes compatible with the estimated small bulk density have a substantial atmosphere that induces a strong greenhouse effect. Alongside tidal heating of its interior, these models show that L 98-59 d presently retains a permanent magma ocean (melt fraction $\Phi \approx 45\%$; Fig. 2f). A solidified mantle is ruled out by ρ_p without invoking the MMW constraint, making this inference insensitive to uncertainties

https://doi.org/10.1038/s41550-026-02815-8

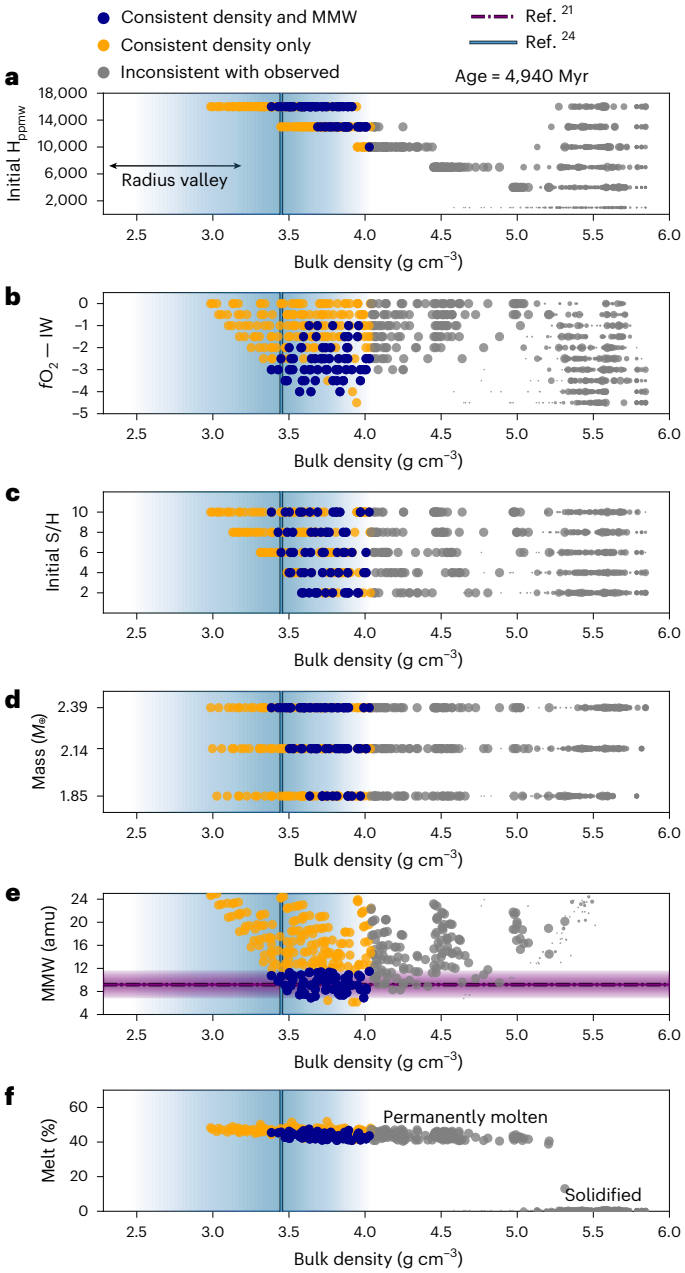

Fig. 2 | Projection of planetary bulk density ρ_p against several variables. Scatter points represent end points of simulations from our grid, projecting the calculated bulk density against other variables: H inventory from formation (**a**), mantle oxygen fugacity (**b**), S/H ratio from formation (**c**), total planet mass (**d**), atmospheric MMW (**e**) and mantle melt fraction (**f**). Point sizes represent the age of the planet at simulation end points; largest scatter-point size corresponds to the present day. Vertical blue line and shaded region ($\pm1\sigma$) highlights the observationally estimated ρ_p. Horizontal purple line shows estimates of MMW (with $\pm1\sigma$ shaded) and H_2S from free-chemistry retrievals. Blue points are consistent with the observed density and MMW; orange points are only consistent with the observed density. amu, atomic mass units; obs., observation.

on the JWST observations and retrievals. The narrow range of mantle melt fractions corresponding to the observed ρ_p is a physical outcome; mantle viscosity increases strongly at $\Phi \lesssim 45\%$ (ref. 37), which makes energy transport through the planet's interior inefficient and thereby allows atmospheric blanketing and tidal heating to keep a permanent magma ocean[28]. In comparison, modelled thin atmospheres lead to mantle solidification (Fig. 2).

Thermal contraction and photoevaporation

Many modelled scenarios initially have large radii on the sub-Neptune side of the radius valley (Fig. 1b). To understand how volatile loss and thermal contraction drive the marked decrease in R_p over time, passing through the radius valley, we study a case compatible with the observations in detail. The case study in Fig. 3 shows L 98-59 d losing 26% of its total volatile inventory while retaining a large surface pressure of 30 kbar (pink bars) at the present day. Some volatiles are degassed during this time due to partial mantle solidification; the majority of the planet's volatiles remain dissolved in the magma ocean. The atmosphere S/H mass ratio increases by a factor of 8.2 because sulfur, which is more soluble than H in silicate melts, is degassed as the magma ocean crystallizes[33,38]. Photoevaporation also drives a relative enhancement in bulk S content due to the favourable interior partitioning of sulfur.

Thermal contraction explains large initial changes in ρ_p. The surface cools from 3,360 K to 1,830 K over the first 1.4 Gyr, corresponding to the effective radius deflating from >2.2 $R_\oplus$ to ~1.74 $R_\oplus$ during that period, despite volatile degassing simultaneously driving a net increase to the surface pressure (Supplementary Fig. 3 and Supplementary Fig. 4). The evolving atmospheric temperature–height profile is visualized in Fig. 3b. Although early atmospheric contraction is an established theoretical behaviour of H_2-dominated envelopes, important in regulating the rate of photoevaporative volatile loss[39,40], here we show that interior cooling is the primary driver of early radius contraction for envelopes for which MMW increases substantially over time. The atmosphere has a deep radiative layer, up to ~5,000 km thick, above which it undergoes dry convection and is then weakly inverted. High temperatures make radiative diffusion efficient at transporting energy[41]. Radiative layers in the deep atmosphere decrease the lapse rate compared to an adiabat, acting to inflate the atmospheric radius for a given surface temperature during the planet's evolution. Prior modelling largely assumed adiabatic or isothermal atmospheres, neglecting this important impact of energy transport on atmospheric structure.

After initial thermal contraction, tidal forces and atmospheric blanketing together sustain a deep magma ocean on L 98-59 d (ref. 28), whereas escape has reduced its radius to its observed value. Importantly, the magma ocean buffers the atmosphere through volatile dissolution into the melt and equilibrium thermochemistry near the surface. It has been previously suggested for H_2O[42] and N compounds[43] that retention of volatiles in deep magma oceans buffers atmospheric escape over deep time, and analogues of Mercurian lavas have established that reducing melts may take up large S inventories[38]. Dissolution of sulfur (Fig. 3a) enables the planet's S inventory to be retained across gigayear timescales and enhances atmospheric S/H over time, as H atoms dominate the escaping outflow. This scenario aligns with Venus/Earth/Mars models in which their present atmosphere masses were largely supplied by magma-ocean degassing[44,45], with later volcanic contributions in uncertain amounts; Archean proxies suggest that early outgassing established most of Earth's present atmospheric mass[46], although its chemistry has changed substantially[47].

Photochemical production of SO_2

Formation of SO_2 from H_2S, in the presence of OH radicals from photolysis H_2O, can explain the detections of SO_2 in L 98-59 d's atmosphere. This mechanism produces SO_2 within the hot-Jupiter WASP-39b[48,49], and SO_2—in the presence of percentage levels of H_2O—has been detected in a Neptune-mass exoplanet[50]. We infer the formation of SO_2 by making a comparison between VULCAN photochemical kinetics models and free-chemistry retrievals[21]. Figure 4 plots atmospheric mixing ratios for our case study under three chemical paradigms: VULCAN SNCHO photochemical kinetics (solid lines), kinetics without photochemistry (dashed lines) and the isochemical volatile outgassing as applied during our evolutionary calculations (triangle markers). The mixing ratio of SO_2 (solid blue line) increases with altitude for $p < 6$ bar, whereas the equivalent case without photochemistry

https://doi.org/10.1038/s41550-026-02815-8

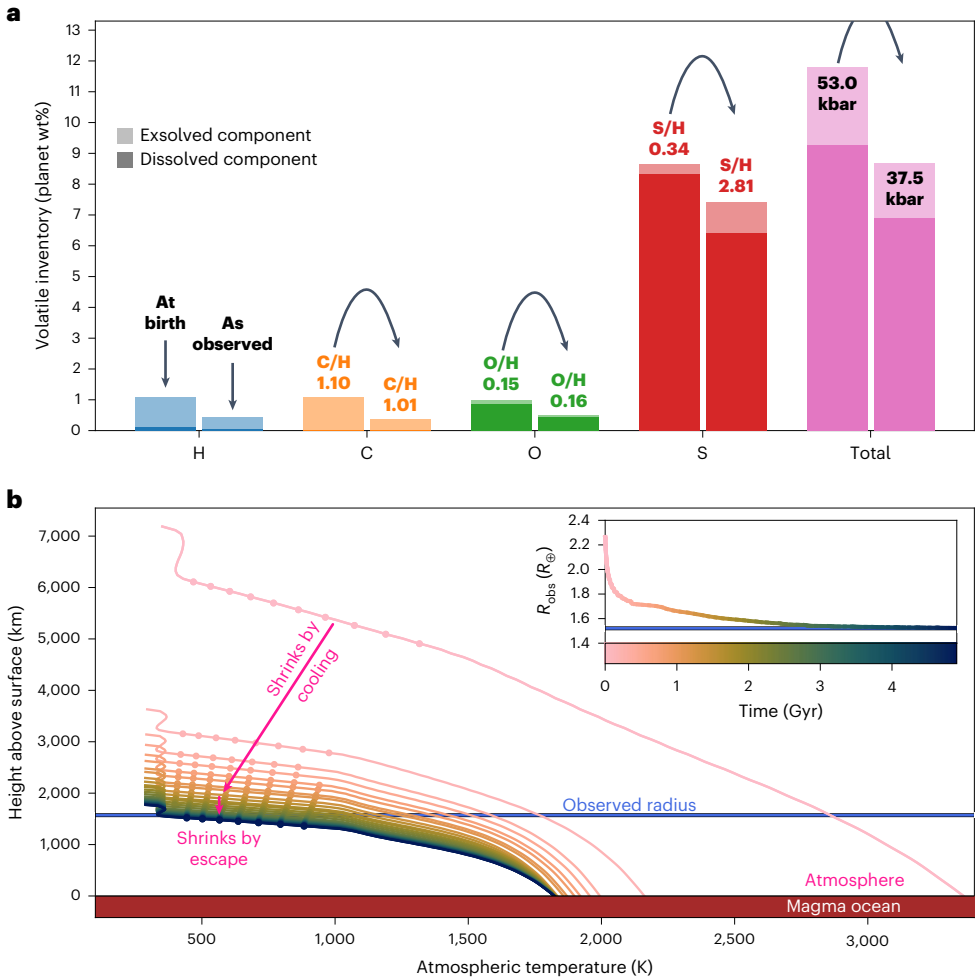

Fig. 3 | Volatile loss and atmosphere contraction over time, through two stages of evolution. Planet bulk density $\rho_p = 3.45$ g cm^{-3} at 4.9 Gyr. **a**, Bar heights highlight the total loss of volatiles between planet birth and observation, as percentages relative to total planet mass. Lighter and darker bar opacities indicate partitioning between the atmosphere and interior, respectively. Atmosphere elemental mass ratios relative to H are annotated. **b**, Visualization of the evolving atmospheric temperature profile, with an initial stage of rapid contraction due to cooling followed by a later stage of slower contraction due to mass loss. Dotted markers indicate convective regions. Profile line colours correspond to time relative to model initialization (colour bar). The colour bar is mapped to the *x* axis of the inset, which plots radius R_p as a function of time.

(dashed blue line) quenches at negligible abundance. Photochemical production of SO_2 is necessary to increase its abundance to that consistent with the JWST observations (error bars). Lime-coloured profiles show that H_2S abundance is consistent with the observational constraints under all three paradigms; H_2S is thermochemically favoured to carry sulfur in the H_2-rich background.

Detections of SO_2 cannot be explained by surface outgassing[28], which would require SO_2 to be transported into the observable upper atmosphere without being thermochemically reduced. Transport of SO_2 (64 g mol^{-1}) would have to take place in the absence of deep convection (Fig. 3b) and therefore only by diffusion through the H_2 background. This physically unlikely scenario instead points to the formation of SO_2 in situ. Production of SO_2 requires the presence of H_2O to form OH radicals; a strongly water-free composition would be physically incompatible with the detection of SO_2. Our photochemical models predict H_2O abundances compatible with the wide observational posterior $\log_{10}\chi_{H_2O} = -6.63^{+4.22}_{-3.51}$ derived by Banerjee et al.[22]. However, an alternative analysis of the same JWST spectrum[21] yields an upper limit of $\log_{10}\chi_{H_2O} < -5$. The abundance of H_2O is poorly constrained by both analyses because H_2O absorption overlaps with multiple features in a common wavelength region. Future observations should robustly check for percent-level H_2O in the atmosphere of L 98-59 d to test for the presence of these photochemical processes. Our comparison with JWST data in Fig. 4 shows that photochemistry actively shapes the observables of super-Earths, dependent on the chemical interactions linking the deep interiors of planets to their upper atmospheres.

Conclusions

Our modelled evolution pathways connect the observed bulk density of L 98-59 d to a narrow range of conditions at birth. Conditions compatible with observations are those in which the planet initially had $\gtrsim$100 times the estimated hydrogen content of the early Earth mantle[35,51]. The majority of L 98-59 d's H and C are stored in its atmosphere, whereas its S remains primarily dissolved within a reducing magma ocean. Hydrogen may also incorporate into the planet's metallic core, allowing additional H storage in bulk and lower core densities[52]. H concentrations up to ~7,300 ppmw at high pressures may allow the majority of Earth's H to be stored in its core[53]. So, although we infer a small core for L 98-59 d, our estimated inventories represent lower limits on volatiles delivered during formation. Fractionation of planetary HCNS inventories between interiors and atmospheres presents an opportunity for testing whether small, low-density exoplanets have underlying magma oceans through measurements of their atmospheric composition[42,43,54].

https://doi.org/10.1038/s41550-026-02815-8

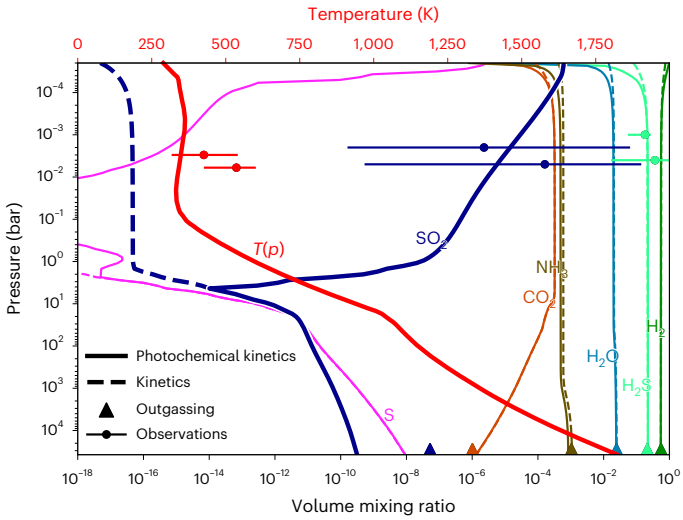

Fig. 4 | Atmospheric composition and temperature profiles. Solid lines plot the volume mixing ratios for a selection of gases calculated with VULCAN's SNCHO photochemical kinetic network. Dashed lines plot mixing ratios calculated without photoreactions. Scatter points show the median estimates for photospheric chemical abundances (blue, lime) and temperatures (red) retrieved by Banerjee et al.[22] and Gressier et al.[21]. Scatter-point error bars represent ±1σ ranges on the JWST retrieval posteriors. We assume a modest eddy diffusion coefficient K_{zz} of 10^5 cm^2 s^{-1} and use the radiative–convective temperature solution obtained by AGNI (thick red line).

L 98-59 d's radius is smaller than that of a prototypical sub-Neptune, although had it been observed at earlier age, $\lesssim$1.4 Gyr, we might have confidently labelled it as one (Fig. 1b). Its transition from the sub-Neptune to super-Earth regime occurs only after several Gyr of thermo-compositional evolution, suggesting that even sub-Neptunes with ages $\gtrsim$1 Gyr may exist in a transient state towards becoming what would later be classified as super-Earths. This Gyr-scale contraction has been suggested to explain radius–age trends in the Kepler survey[3] as an alternative to the 'loss and revival' mechanism[55].

L 98-59 d currently has a radius commensurate with a super-Earth planet in the vicinity of the radius valley, but its low bulk density necessitates that it comprises substantial volatiles. A modestly large atmospheric MMW means that it is not an evolved gas dwarf with a primitive atmosphere sourced from protoplanetary disk gas; a water-world scenario is also not required to explain its current bulk properties. Moreover, forming a substantially water-dominated atmosphere would require oxidizing conditions incompatible with the MMW inferred from JWST transmission spectroscopy, pointing to geochemical conditions in the interior of L 98-59 d that are unknown from the Solar System. Instead, global-scale disequilibrium evolution driven by thermal contraction, magma-ocean degassing, tidal heating, photochemistry and photoevaporative mass loss have together continuously shaped the radius and atmospheric composition of L 98-59 d over its lifetime.

Methods

Modelling framework

We use PROTEUS to simulate the time evolution of L 98-59 up to the present day[25,26,28]. PROTEUS is a self-consistently coupled modular simulation framework that links the SPIDER interior evolution model[56,57] and the AGNI radiative–convective atmosphere model[27,58]. The atmospheric composition is determined by equilibrium thermochemistry and the solubility of volatiles into the magma ocean[33,59]. Volatiles are assumed to partition between the partially molten mantle and overlying atmosphere at solubility equilibrium, subject to mass conservation and the two-phase dynamics and crystallization of the mantle at each point in time. The total planetary inventory of CHNS volatiles is initialized via our model parameters; compare to Supplementary Fig. 5. We assume that the stellar nebula has already dispersed, and no primary-accreted atmosphere remnant is considered. However, the planet's volatile inventory continually evolves due to removal by hydrodynamic escape and redox reactions of O with Fe in the mantle, set by the temperature-dependent IW buffer reaction. Partitioning of volatiles into solid phases[60–62] and volcanic outgassing[63] are not included in the model, as all cases of interest retain magma oceans; volcanic mass fluxes associated with a solidified interior are several orders of magnitude below those from efficient magma-ocean degassing[1,64,65]. The mantle material itself is chemically inert.

The pure-$MgSiO_3$ molten mantle is initialized on an adiabat and evolved over time by SPIDER according to the energy fluxes at each radial level. The initial specific entropy is set to 3,150 J K^{-1}kg^{-1}; the planet's subsequent evolution is insensitive to this exact value. Mixing-length theory convection, solid–liquid phase separation, grain gravitational settling, radiogenic heating, core cooling and tidal heating are modelled self-consistently. Tidal heating profiles are calculated using LOVEPY[66] under a Maxwell viscoelastic rheology; the depth-dependent density, shear modulus, bulk modulus and shear viscosity are calculated from the melt fraction profiles solved by SPIDER using empirical scaling relations[67]. Application of more realistic rheological parametrizations would yield increased tidal heat fluxes and thus hotter and more molten interiors[68,69]. As in several previous studies (for example, refs. 25,26,34,57,70,71) we do not spatially resolve energy transport within the metallic core and instead fix its bulk density and heat capacity to representative Earth-like[72] values of 10.738 g cm^{-3} and 880 J K^{-1} kg^{-1} following ref. 56. A pure Fe core of the same relative radius would be denser in L 98-59 d compared to Earth, due to compression by mantle overburden pressure, although the compression would be offset by incorporation of lighter elements (SNCHO, and so on) into the core, decreasing its density compared to pure Fe[73,74]. Sensitivity tests assess the impact of this interior structure assumption on our results (Supplementary Fig. 2). Heat is transported across the core–mantle boundary following ref. 75. SPIDER uses the Wolf and Bower[76] EOS for $MgSiO_3$ melt; mantle density is independent of dissolved volatile content, which can be neglected in the modelled regime[42]. The core radius is nominally fixed at 55% of the interior radius (see the sensitivity test in Supplementary Fig. 2g), consistent with the relative size of Earth's core[77], although alternative estimates of the planet's density permit theoretically constraining the planet's core size (Supplementary Fig. 1). The radius $R_{\rm int}$ of the planet's interior (mantle plus core) is calculated using SPIDER by solving for its hydrostatic structure for a given interior mass $M_{\rm int} = M_{\rm p} - M_{\rm atm}$. For a planet mass $M_{\rm p} = 2.14\,M_{\oplus}$, we obtain $M_{core} = 3.9 \times 10^{24}\,kg = 0.66 M_{\oplus}$ and $M_{\rm mant} = 8.85 \times 10^{24}$ kg $= 1.48\,M_{\oplus}$. The interior radius $R_{\rm int}$ is held constant throughout each simulation; thermal contraction and mantle solidification do not chiefly affect the volume of silicate mantles[1,78,79].

Energy transport through an optically thick atmosphere regulates the planet's energy balance. At each time step, our radiative–convective atmosphere model AGNI calculates the net atmospheric energy flux for the outgassed chemical composition, instellation flux and top-of-mantle temperature. The radiation fluxes at each atmosphere level are calculated using SOCRATES[80,81] correlated-k two-stream ($\theta_{\rm zen} = 54.74^{\circ}$) radiative transfer with 48 spectral bands, including Rayleigh scattering and non-grey basaltic surface emissivity. Schwarzschild-stable mixing-length theory[82] is applied to calculate the convective energy flux. An energy-conserving atmospheric solution is obtained using the Newton–Raphson method with line search. The incorporation of a real-gas EOS formulation into AGNI is presented in Supplementary Fig. 6.

Evolution of stellar radius, bolometric luminosity and photometric emission is modelled using MORS[83]. We take L 98-59 to have a mass of 0.273 $M_{\odot}$ and present-day rotation rate of 80.9 days in our main grid of models[84]. MORS uses a two-shell rotational evolution

calculation with empirically derived scalings to estimate the bolometric and XUV emission from the star over its lifetime. Using this established code, the estimated X-ray luminosity at the present day is consistent with XMM-Newton observations of L 98-59 (refs. 28,85). We use the L 98-59 spectrum from the MUSCLES Extension[85]. Stellar quantities are updated throughout the simulations; changes in stellar flux are thus reflected in the atmospheric temperature profile, albedo and escape rate.

All simulations are initialized at a planet age of $t_{ini} = 50$ Myr relative to the formation of the system under the assumption that boil-off has completed[86] and further delivery processes are negligible compared to the physics and timescales simulated[87]. Simulations terminate when the simulated age reaches the 4.94-Gyr estimated age of L 98-59 (ref. 84) or when the mantle solidifies (mass melt fraction $\Phi < 0.5\%$). Cases consistent with the observations are those with a planet bulk density ρ_p comparable ($\pm 1\sigma$) to an estimated density of 3.45 g cm^{-3} in our main results[24]. A recent radial-velocity and transit-timing reanalysis has yielded a even lower bulk density of 2.2 g cm^{-3} (ref. 20); our comparison with the previous higher estimate of ρ_p (Fig. 2) thereby yields conservatively lower estimates for total volatile content. We compare our models to these new estimates in Supplementary Fig. 1. $\rho_p = 3M_p/4\pi R_p^3$ depends on the total planet mass M_p and the observable radius R_p that would effectively be probed by transit measurements. M_p includes the mantle, metallic core, dissolved volatiles and atmosphere. The modelled observable radius R_p is determined by the radius corresponding to the 20 mbar pressure level[30], to which our results are not sensitive.

Energy-limited escape

Atmospheric escape is modelled within the PROTEUS framework using the classic energy-limited formulation of photoevaporative mass loss

$$\mathring{M}_{esc}(t) = \frac{\eta\pi[R_{XUV}(t)]^3 F_{XUV}(t)}{GM_p}, \quad (1)$$

which assumes that stellar XUV flux F_{XUV} absorbed by an optically thick disk of radius R_{XUV} lifts mass (kg s^{-1}) at a rate M_{esc} out of the gravitational potential well with efficiency η, at each point in time t. The time-dependent $F_{XUV}(t)$ is calculated with MORS[83]. $R_{XUV}(t)$ is determined from the atmospheric temperature structures calculated by AGNI (Supplementary Information), taking $P_{XUV} = 5$ Pa (ref. 30).

An atmosphere composed of hydrogen and high-MMW elements will experience compositional fractionation at varying degrees depending on the XUV irradiation, collisional coupling between species, and gravity. In the limit of rapid hydrodynamic escape and where the high-MMW elements compose a substantial fraction of the atmosphere by mass, hydrodynamic simulations from ref. 88 have shown that the thermosphere is expected to escape in bulk without fractionating. Here, we explore high-MMW atmospheres exposed to XUV fluxes greater than 100 times present Earth levels, so we adopt this approximation of no thermospheric fractionation. Including fractionation in our model of escape would not change our major conclusions, as it would only enhance the S/H ratio.

We adopt a 10% escape efficiency[6,30], which agrees with simulations from ref. 89 that account for molecular line cooling; see also the sensitivity tests in Supplementary Figs. 2 and 7. The elemental composition of the escaping gas is set equal to that of the outgassed atmosphere, which would be photodissociated and partially photoionized on outflow. To calculate the loss rate of each element from the planet's total volatile inventory, we proportion the bulk escape rate by the atmospheric mass mixing ratios of each element. So, although the escape process itself is treated as non-fractionating, it acts upon an atmospheric elemental composition different to the bulk planetary composition. Volatile loss thereby fractionates the planet's elemental inventories as a result of the interior-atmosphere partitioning of HCNS elements.

Data availability

The simulation data and simulation codes underlying this article are available via Zenodo at https://doi.org/10.5281/zenodo.17368256 (ref. 90).

Code availability

In addition to the archive available via Zenodo at https://doi.org/10.5281/zenodo.17368256 (ref. 90), all computer codes used in this work are open source software available via GitHub: PROTEUS, https://github.com/FormingWorlds/PROTEUS; AGNI, https://github.com/nichollsh/AGNI; SPIDER, https://github.com/djbower/spider; LOVEPY, https://github.com/nichollsh/lovepy and SOCRATES, https://github.com/nichollsh/SOCRATES.

References

1. Lichtenberg, T. & Miguel, Y. in *Treatise on Geochemistry* 3rd edn., Vol. 7 (eds Anbar, A. & Weis, D.) Ch. 3 (Elsevier, 2025).
2. Fulton, B. J. & Petigura, E. A. The California-*Kepler* Survey. VII. Precise planet radii leveraging *Gaia* DR2 reveal the stellar mass dependence of the planet radius gap. *Astron. J.* **156**, 264 (2018).
3. David, T. J. et al. Evolution of the exoplanet size distribution: forming large super-earths over billions of years. *Astron. J.* **161**, 265 (2021).
4. Valencia, D., Moro-Martin, A. & Teske, J. in *Treatise on Geochemistry* 3rd edn., Vol. 7 (eds Anbar, A. & Weis, D.) Ch. 2 (Elsevier, 2025).
5. Zeng, L. et al. Growth model interpretation of planet size distribution. *Proc. Natl Acad. Sci. USA* **116**, 9723–9728 (2019).
6. Owen, J. E. Atmospheric escape and the evolution of close-in exoplanets. *Annu. Rev. Earth Planet. Sci.* **47**, 67–90 (2019).
7. Lopez, E. D. Born dry in the photoevaporation desert: Kepler's ultra-short-period planets formed water-poor. *Mon. Not. R. Astron. Soc.* **472**, 245–253 (2017).
8. Mousis, O. et al. Irradiated ocean planets bridge super-earth and sub-neptune populations. *Astrophys. J. Lett.* **896**, 22 (2020).
9. Luque, R. & Palle, E. Density, not radius, separates rocky and water-rich small planets orbiting M dwarf stars. *Science* **377**, 1211–1214 (2022).
10. Lacedelli, G. et al. Investigating the architecture and internal structure of the Toi-561 system planets with Cheops, Harps-n, and Tess. *Mon. Not. R. Astron. Soc.* **511**, 4551–4571 (2022).
11. Burn, R. et al. A radius valley between migrated steam worlds and evaporated rocky cores. *Nat. Astron.* **8**, 463–471 (2024).
12. Bean, J. L., Raymond, S. N. & Owen, J. E. The nature and origins of sub-Neptune size planets. *J. Geophys. Res. Planets* **126**, e2020JE006639 (2021).
13. Rogers, J. G. On the road to the radius valley: distinguishing between gas dwarfs and water worlds with young transiting exoplanets. *Mon. Not. R. Astron. Soc.* **539**, 2230–2241 (2025).
14. Fernandes, R. B. et al. Signatures of atmospheric mass loss and planet migration in the time evolution of short-period transiting exoplanets. *Astron. J.* **169**, 208 (2025).
15. Demangeon, O. D. S. et al. Warm terrestrial planet with half the mass of Venus transiting a nearby star. *Astron. Astrophys.* **653**, 41 (2021).
16. Kostov, V. B. et al. The L 98-59 system: three transiting, terrestrial-size planets orbiting a nearby M dwarf. *Astron. J.* **158**, 32 (2019).
17. Zhou, L., Ma, B., Wang, Y. & Zhu, Y. Hubble WFC3 spectroscopy of the rocky planet L 98-59 b: no evidence for a cloud-free primordial atmosphere. *Astron. J.* **164**, 203 (2022).
18. Bello-Arufe, A. et al. Evidence for a volcanic atmosphere on the sub-Earth L 98-59 b. *Astrophys. J. Lett.* **980**, L26 (2025).
19. Zhou, L., Ma, B., Wang, Y.-H. & Zhu, Y.-N. Hubble WFC3 spectroscopy of the terrestrial planets L 98-59 c and d: no evidence for a clear hydrogen dominated primary atmosphere. *Res. Astron. Astrophys.* **23**, 025011 (2023).

20. Cadieux, C. et al. Detailed architecture of the L 98-59 system and confirmation of a fifth planet in the habitable zone. *Astron. J.* **170**, 154 (2025).
21. Gressier, A. et al. Hints of a sulfur-rich atmosphere around the 1.6 $R_\oplus$ super-Earth L98-59 d from JWST NIRspec G395H transmission spectroscopy. *Astrophys. J. Lett.* **975**, 10 (2024).
22. Banerjee, A. et al. Atmospheric retrievals suggest the presence of a secondary atmosphere and possible sulfur species on l98-59 d from JWST nirspec g395h transmission spectroscopy. *Astrophys. J. Lett.* **975**, 11 (2024).
23. Parc, L., Bouchy, F., Venturini, J., Dorn, C. & Helled, R. From super-Earths to sub-Neptunes: observational constraints and connections to theoretical models. *Astron. Astrophys.* **688**, 59 (2024).
24. Rajpaul, V. M., Barragán, O. & Zicher, N. A non-zero Doppler amplitude is not enough: revisiting the putative radial velocity detection of sub-Venus exoplanet L 98-59b. *Mon. Not. R. Astron. Soc.* **530**, 4665–4675 (2024).
25. Lichtenberg, T. et al. Vertically resolved magma ocean-protoatmosphere evolution: H_2, H_2O, CO_2, CH_4, CO, O_2, and N_2 as PRIMARY ABSORBERS. *J. Geophys. Res.: Planets* **126**, e2020JE006711 (2021).
26. Nicholls, H., Lichtenberg, T., Bower, D. J. & Pierrehumbert, R. Magma ocean evolution at arbitrary redox state. *J. Geophys. Res.: Planets* **129**, e2024JE008576 (2024).
27. Nicholls, H., Pierrehumbert, R. T., Lichtenberg, T., Soucasse, L. & Smeets, S. Convective shutdown in the atmospheres of lava worlds. *Mon. Not. R. Astron. Soc.* **536**, 2957–2971 (2024).
28. Nicholls, H. et al. Self-limited tidal heating and prolonged magma oceans in the L 98-59 system. *Mon. Not. R. Astron. Soc.* **541**, 2566–2584 (2025).
29. Innes, H., Tsai, S.-M. & Pierrehumbert, R. T. The runaway greenhouse effect on hycean worlds. *Astrophys. J.* **953**, 168 (2023).
30. Lehmer, O. R. & Catling, D. C. Rocky worlds limited to 1.8 earth radii by atmospheric escape during a star's extreme UV saturation. *Astrophys. J.* **845**, 130 (2017).
31. Venturini, J. et al. The nature of the radius valley. Hints from formation and evolution models. *Astron. Astrophys.* **643**, 1 (2020).
32. Righter, K., Sutton, S. R., Danielson, L., Pando, K. & Newville, M. Redox variations in the inner solar system with new constraints from vanadium XANES in spinels. *Am. Mineral.* **101**, 1928–1942 (2016).
33. Gaillard, F. et al. Redox controls during magma ocean degassing. *Earth Planet. Sci. Lett.* **577**, 117255 (2022).
34. Krissansen-Totton, J., Wogan, N., Thompson, M. & Fortney, J. J. The erosion of large primary atmospheres typically leaves behind substantial secondary atmospheres on temperate rocky planets. *Nat. Commun.* **15**, 8374 (2024).
35. Krijt, S. et al. in *Protostars and Planets VII* (eds Inutsuka, S. et al.) Ch. 28 (Astronomical Society of the Pacific, 2023).
36. Owen, J. E. & Wu, Y. The evaporation valley in the Kepler planets. *Astrophys. J.* **847**, 29 (2017).
37. Costa, A., Caricchi, L. & Bagdassarov, N. A model for the rheology of particle-bearing suspensions and partially molten rocks. *Geochem. Geophys. Geosys.* **10**, Q03010 (2009).
38. Namur, O., Charlier, B., Holtz, F., Cartier, C. & McCammon, C. Sulfur solubility in reduced mafic silicate melts: implications for the speciation and distribution of sulfur on mercury. *Earth Planet. Sci. Lett.* **448**, 102–114 (2016).
39. Kubyshkina, D., Vidotto, A. A., Fossati, L. & Farrell, E. Coupling thermal evolution of planets and hydrodynamic atmospheric escape in mesa. *Mon. Not. R. Astron. Soc.* **499**, 77–88 (2020).
40. Lopez, E. D. & Fortney, J. J. Understanding the mass-radius relation for sub-neptunes: radius as a proxy for composition. *Astrophys. J.* **792**, 1 (2014).
41. Pierrehumbert, R. *Principles of Planetary Climate* (Cambridge Univ. Press, 2010).
42. Dorn, C. & Lichtenberg, T. Hidden water in magma ocean exoplanets. *Astrophys. J. Lett.* **922**, 4 (2021).
43. Shorttle, O., Jordan, S., Nicholls, H., Lichtenberg, T. & Bower, D. J. Distinguishing oceans of water from magma on mini-Neptune k2-18b. *Astrophys. J. Lett.* **962**, 8 (2024).
44. Elkins-Tanton, L. T. Magma oceans in the inner solar system. *Annu. Rev. Earth Planet. Sci.* **40**, 113–139 (2012).
45. Hirschmann, M. M. Magma ocean influence on early atmosphere mass and composition. *Earth Planet. Sci. Lett.* **341-344**, 48–57 (2012).
46. Marty, B., Zimmermann, L., Pujol, M., Burgess, R. & Philippot, P. Nitrogen isotopic composition and density of the Archean atmosphere. *Science* **342**, 101–104 (2013).
47. Halliday, A. N. & Canup, R. M. The accretion of planet earth. *Nat. Rev. Earth Environ.* **4**, 19–35 (2023).
48. Tsai, S.-M. et al. Photochemically produced SO2 in the atmosphere of WASP-39b. *Nature* **617**, 483–487 (2023).
49. Powell, D. et al. Sulfur dioxide in the mid-infrared transmission spectrum of wasp-39b. *Nature* **626**, 979–983 (2024).
50. Gressier, A. et al. JWST-TST DREAMS: sulfur dioxide in the atmosphere of the Neptune-mass planet hat-p-26 b from nirspec g395h transmission spectroscopy. *Astron. J.* **170**, 292 (2025).
51. Wang, H. S., Lineweaver, C. H. & Ireland, T. R. The elemental abundances (with uncertainties) of the most earth-like planet. *Icarus* **299**, 460–474 (2018).
52. Wade, J. & Wood, B. J. Core formation and the oxidation state of the Earth. *Earth Planet. Sci. Lett.* **236**, 78–95 (2005).
53. Peslier, A. H., Schonbachler, M., Busemann, H. & Karato, S.-I. Water in the earth's interior: distribution and origin. *Space Sci. Rev.* **212**, 743–810 (2017).
54. Kite, E. S., Fegley Jr, B. F., Schaefer, L. & Gaidos, E. Atmosphere-interior exchange on hot, rocky exoplanets. *Astrophys. J.* **828**, 80 (2016).
55. Kite, E. S. & Barnett, M. N. Exoplanet secondary atmosphere loss and revival. *Proc. Natl Acad. Sci. USA* **117**, 18264–18271 (2020).
56. Bower, D. J., Sanan, P. & Wolf, A. S. Numerical solution of a non-linear conservation law applicable to the interior dynamics of partially molten planets. *Phys. Earth Planet. Inter.* **274**, 49–62 (2018).
57. Bower, D. J., Hakim, K., Sossi, P. A. & Sanan, P. Retention of water in terrestrial magma oceans and carbon-rich early atmospheres. *Planet. Sci. J.* **3**, 93 (2022).
58. Nicholls, H., Pierrehumbert, R. & Lichtenberg, T. Agni: a radiative-convective model for lava planet atmospheres. *J. Open Source Softw.* **10**, 7726 (2025).
59. Sossi, P. A., Tollan, P. M. E., Badro, J. & Bower, D. J. Solubility of water in peridotite liquids and the prevalence of steam atmospheres on rocky planets. *Earth Planet. Sci. Lett.* **601**, 117894 (2023).
60. Hier-Majumder, S. & Hirschmann, M. M. The origin of volatiles in the earth's mantle. *Geochem. Geophys. Geosys.* **18**, 3078–3092 (2017).
61. Sim, S. J., Hirschmann, M. M. & Hier-Majumder, S. Volatile and trace element storage in a crystallizing martian magma ocean. *J. Geophys. Res.: Planets* **129**, e2024JE008346 (2024).
62. Guimond, C. M., Shorttle, O. & Rudge, J. F. Mantle mineralogy limits to rocky planet water inventories. *Mon. Not. R. Astron. Soc.* **521**, 2535–2552 (2023).
63. Liggins, P., Jordan, S., Rimmer, P. B. & Shorttle, O. Growth and evolution of secondary volcanic atmospheres: I. Identifying the geological character of hot rocky planets. *J. Geophys. Res. Planets* **127**, e2021JE007123 (2022).

64. Gaillard, F. et al. The diverse planetary ingassing/outgassing paths produced over billions of years of magmatic activity. *Space Sci. Rev.* **217**, 22 (2021).
65. Guimond, C. M., Noack, L., Ortenzi, G. & Sohl, F. Low volcanic outgassing rates for a stagnant lid Archean earth with graphite-saturated magmas. *Phys. Earth Planet. Inter.* **320**, 106788 (2021).
66. Hay, H. C. F. C., Trinh, A. & Matsuyama, I. Powering the Galilean satellites with moon-moon tides. *Geophys. Res. Lett.* **47**, 88317 (2020).
67. Kervazo, M. et al. Solid tides in Io's partially molten interior - contribution of bulk dissipation. *Astron. Astrophys.* **650**, 72 (2021).
68. Renaud, J. P. & Henning, W. G. Increased tidal dissipation using advanced rheological models implications for Io and tidally active exoplanets. *Astrophys. J.* **857**, 98 (2017).
69. Farhat, M., Auclair-Desrotour, P., Boué, G., Lichtenberg, T. & Laskar, J. Tides on lava worlds: application to close-in exoplanets and the early earth–moon system. *Astrophys. J.* **979**, 133 (2025).
70. Hamano, K., Kawahara, H., Abe, Y., Onishi, M. & Hashimoto, G. L. Lifetime and spectral evolution of a magma ocean with a steam atmosphere: its detectability by future direct imaging. *Astrophys. J.* **806**, 216 (2015).
71. Schaefer, L., Wordsworth, R. D., Berta-Thompson, Z. & Sasselov, D. Predictions of the atmospheric composition of gj 1132b. *Astrophys. J.* **829**, 63 (2016).
72. Dziewonski, A. M. & Anderson, D. L. Preliminary reference earth model. *Phys. Earth Planet. Inter.* **25**, 297–356 (1981).
73. Luo, H., Dorn, C. & Deng, J. The interior as the dominant water reservoir in super-earths and sub-neptunes. *Nat. Astron.* **8**, 1399–1407 (2024).
74. Hirose, K., Wood, B. & Vocadlo, L. Light elements in the earth's core. *Nat. Rev. Earth Environ.* **2**, 645–658 (2021).
75. Bower, D. J. et al. Linking the evolution of terrestrial interiors and an early outgassed atmosphere to astrophysical observations. *Astron. Astrophys.* **631**, 103 (2019).
76. Wolf, A. S. & Bower, D. J. An equation of state for high pressure-temperature liquids (rtpress) with application to mgsio3 melt. *Phys. Earth Planet. Inter.* **278**, 59–74 (2018).
77. Lodders, K. & Fegley, B. *The Planetary Scientist's Companion* (Oxford Univ. Press, 1998).
78. Boley, K. M. et al. Fizzy super-earths: impacts of magma composition on the bulk density and structure of lava worlds. *Astrophys. J.* **954**, 202 (2023).
79. Unterborn, C. T. & Panero, W. R. The pressure and temperature limits of likely rocky exoplanets. *J. Geophys. Res. Planets* **124**, 1704–1716 (2019).
80. Edwards, J. M. & Slingo, A. Studies with a flexible new radiation code. I: Choosing a configuration for a large-scale model. *Q. J. R. Meteorol. Soc.* **122**, 689–719 (1996).
81. Amundsen, D. et al. Accuracy tests of radiation schemes used in hot Jupiter global circulation models. *Astron. Astrophys.* **564**, 59 (2014).
82. Joyce, M. & Tayar, J. A review of the mixing length theory of convection in 1D stellar modeling. *Galaxies* **11**, 75 (2023).
83. Johnstone, C. P., Bartel, M. & Gudel, M. The active lives of stars: a complete description of the rotation and XUV evolution of F, G, K, and M dwarfs. *Astron. Astrophys.* **649**, 96 (2021).
84. Engle, S. G. & Guinan, E. F. Living with a red dwarf: the rotation-age relationships of m dwarfs. *Astrophys. J. Lett.* **954**, 50 (2023).
85. Behr, P. R. et al. The MUSCLES extension for atmospheric transmission spectroscopy: UV and X-ray host-star observations for JWST ERS & GTO targets. *Astron. J.* **166**, 35 (2023).
86. Tang, Y., Fortney, J. J. & Murray-Clay, R. Assessing core-powered mass loss in the context of early boil-off: minimal long-lived mass loss for the sub-neptune population. *Astrophys. J.* **976**, 221 (2024).
87. Lichtenberg, T. et al. in *Protostars and Planets VII* (eds Inutsuka, S. et al.) Ch. 25 (Astronomical Society of the Pacific, 2023).
88. Johnstone, C. P. Hydrodynamic escape of water vapor atmospheres near very active stars. *Astrophys. J.* **890**, 79 (2020).
89. Yoshida, T., Terada, N. & Kuramoto, K. Suppression of hydrodynamic escape of an H2-rich early earth atmosphere by radiative cooling of carbon oxides. *Prog. Earth Planet. Sci.* **11**, 59 (2024).
90. Nicholls, H. Volatile-rich evolution of molten super-Earth L 98-59 d (simulations and code). *Zenodo* https://doi.org/10.5281/zenodo.17368256 (2025)

Acknowledgements

T.L. acknowledges support from the Netherlands eScience Center (PROTEUS project, grant no. NLESC.OEC.2023.017), the Branco Weiss Foundation, the Alfred P. Sloan Foundation (AEThER project, grant no. G-2025-25284) and NASA's Nexus for Exoplanet System Science research coordination network (Alien Earths project, grant no. 80NSSC21K0593). C.M.G. is supported by the UK STFC (grant no. ST/W000903/1). R.T.P. and R.D.C. acknowledge support from the UK STFC and the AEThER project. R.D.C. also thanks UKRI for their support via grant no. UKRI1191. We thank the Center for Information Technology of the University of Groningen for their support and for providing access to the Habrok high-performance computing cluster. We also thank T. Komacek for his suggestions on this manuscript and L. Soucasse for his contributions to PROTEUS.

Author contributions

H.N.: Conceptualization, methodology, software, investigation, writing—original draft, writing—review and editing, visualization. T.L.: Conceptualization, methodology, software, writing—review and editing. R.D.C.: Conceptualization, methodology, writing—original draft. C.M.G.: Conceptualization, writing—review and editing. EP: Software, writing—review and editing. R.T.P.: Supervision.

Competing interests

The authors declare no competing interests.

Additional information

Supplementary information The online version contains supplementary material available at https://doi.org/10.1038/s41550-026-02815-8.

Correspondence and requests for materials should be addressed to Harrison Nicholls.

Peer review information *Nature Astronomy* thanks the anonymous reviewers for their contribution to the peer review of this work. Peer reviewer reports are available.